Voltage control of patterned metal/insulator properties in oxide/oxyfluoride lateral perovskite heterostructures *via* ion gel gating

Benjamin M. Lefler[1], William M. Postiglione[2], Chris Leighton[2], and Steven J. May[1,]*

B. M. Lefler, S. J. May
Department of Materials Science and Engineering
Drexel University
Philadelphia, PA 19104, USA
E-mail: smay@drexel.edu

W. M. Postiglione, C. Leighton
Department of Chemical Engineering and Materials Science
University of Minnesota
Minneapolis, MN 55455, USA

Keywords: perovskites, ionic gating, topochemistry, heterostructures

Dynamic control of patterned properties in perovskite oxide films could enable new architectures for electronic, magnetic, and optical devices. In this work, we show that $SrFeO_{3-\delta}$/$SrFeO_2F$ laterally-heterostructured films enable voltage-controlled tunable and reversible metal-insulator patterned properties using room-temperature ion gel gating. Specifically, $SrFeO_{3-\delta}$ film regions can be toggled between insulating $H_xSrFeO_{2.5}$ and metallic $SrFeO_3$ by electrochemical redox, while $SrFeO_2F$ regions remain robustly insulating and are unaffected by ion gel gating. We also compare various gating architectures and establish the advantages of employing a conductive substrate as the contacting electrode, as opposed to at the film surface, thereby achieving complete and reversible reduction and oxidation among $SrFeO_{3-\delta}$, $H_xSrFeO_{2.5}$, and $SrFeO_3$. This approach to voltage-modulated patterned electronic, optical, and magnetic properties should be broadly applicable to oxide materials amenable to fluoridation, and potentially other forms of anion substitution.

1. Introduction

Perovskite oxides - with the formula ABO_3 in which A = alkali, alkaline earth, or rare earth cation(s), and B = transition metal cation(s) - offer a rich landscape of electronic, magnetic, and optical properties. These properties are statically tunable *via* composition, *i.e.*, the identity (and alloying) of the *B*-site transition metal as well as modification of its oxidation state through *A*-site substitutional charge compensation. *Dynamical* control of properties, however, could realize entirely new device applications for these materials. One major current paradigm in device engineering relies on voltage control of semiconductors for switchable behavior. In the ubiquitous field-effect transistor, for example, this is achieved by applying an electric field across a gate insulator interfaced with the active material, to modulate the interfacial charge-carrier population. However, due to the high carrier densities and short screening lengths of perovskite oxides, this typical dielectric gating approach is not viable[1,2]. As an alternative to conventional gate dielectrics, electrolyte-based ionic gating has been demonstrated for electric-field-based modulation of perovskite properties[1,2].

In ionic gating, an ion-conducting dielectric is used as the gating medium, which responds to external bias *via* motion of ions through the material, thus accumulating ionic charge at the electrolyte-perovskite interface. This can be achieved at room temperature often using high-ion-mobility ionic liquids or solid-state ion gels (ionic liquids suspended in polymer matrices)[3], though polymer[4], nanoporous glassy oxide[5,6], and composite resin[7,8] alternatives have also been reported. Upon gating, the electrolyte/perovskite interface acts as an electric double-layer capacitor, capable of achieving very high local electric fields at low applied bias[2]. This architecture has been used for strong *electrostatic* modulation of various materials, including perovskite oxides[1,2,9]. However, particularly effective control over magnetic, electronic, and optical function can also be realized through *electrochemical* gating of perovskites, in which the interfacial electric field reduces and oxidizes the perovskite through the removal and re-insertion of oxygen ions. The precise mechanism of this electrochemistry has not been explained in full, although hypothesized mechanisms point to either molecular oxygen[10,11] or water[7,12–14] as the source and sink for the lattice O^{2-}. Electrochemical gating of this nature has attracted particular attention for neuromorphic[1,2,15,16], magneto-ionic[1,2,17–19], and electrochromic[20] device applications. Numerous $ABO_{3-\delta}$ perovskites support such electrochemical dynamic and reversible tunability of properties through control of the oxygen deficiency, where δ can be as high as 0.5. Due to charge compensation, oxygen deficiency alters the *B*-site cation oxidation state, thereby reversibly modulating properties. Electrochemical control of oxygen vacancies using ionic gating has thus been demonstrated to tune the electronic,

magnetic, and/or optical properties of cobaltites[7,12,13,21–27], manganites[23,28,29], nickelates[30,31], and ferrites[8,24,32–34], to name just a few examples in the field of oxide perovskites, as well as phenomena stemming from interlayer interactions in perovskite vertical heterostructures[33,35] and properties of various other oxides[1]. While this oxygen vacancy modulation is a key pathway toward electrochemical control of properties in oxides, electrochemical manipulation *via* other ions is also effective, such as in the case of voltage-driven shuttling of hydrogen[4,12–14,36–38] and nitrogen[39]. Importantly, in contrast to electrostatic gating, these electrochemical effects are not limited by an interfacial electrostatic screening length. The electrochemical approach can thus transform a material over a depth of tens of unit cells, often the full film thickness, depending on the ionic diffusivity. It should be emphasized, however, that the capability to oxidize or reduce selective *lateral* regions of a uniformly-gated material is yet to be demonstrated, despite the prominent role that laterally-patterned materials play in a wide range of optical, electronic, and magnetic applications.

In this work, we demonstrate a new approach, establishing voltage control of laterally-patterned structures by taking advantage of the markedly different responses to electrolyte gating of $SrFeO_{3-\delta}$ and $SrFeO_2F$, which we pattern in-plane using a combination of photolithography and vapor-based topochemistry. We utilize $SrFeO_{3-\delta}$, which supports oxygen deficiency in the range $0 \leq \delta \leq 0.5$, as a model system but the general strategy should be broadly applicable to any oxide family that can be topochemically transformed to oxyfluorides. Fully oxidized $SrFeO_3$ is a helimagnetic, metallic material with perovskite structure, while the analogous reduced $SrFeO_{2.5}$ is an antiferromagnetic highly-resistive semiconductor (2.3 eV band gap) with the oxygen-vacancy-ordered brownmillerite crystal structure[40–47]. The room temperature resistivities of the $\delta = 0$ and $\delta = 0.5$ phases differs by 9 orders of magnitude[40], making $SrFeO_{3-\delta}$ an attractive material for electrical switching devices[48], of particular interest for neuromorphic applications[34]. In our previous work[49], we demonstrated the ability to combine photolithographic patterning with low-temperature solid-vapor fluoridation and redox chemistries to generate patterned films of $SrFeO_3$, $SrFeO_{2.5}$, and $SrFeO_2F$ (a highly-resistive semiconducting perovskite phase[50]), demonstrating that under oxidative and reductive annealing environments, the oxyfluoride phase remains robust to further property modifications. Herein we show that $SrFeO_2F$ is also robust against electrochemical modulation by ion gel gating, enabling voltage-driven metal-insulator transformations to proceed within $SrFeO_{3-\delta}$ patterned regions while retaining semiconducting $SrFeO_2F$ regions. These results demonstrate the promise of combining fluoridation chemistry with electrolytic gating to realize voltage-control of optoelectronic patterns of oxide lateral heterostructures.

2. Results and Discussion

We first determined the voltage-dependent electrochemical effects resulting from ion gel-gating of monolithic films of $SrFeO_{3-\delta}$ and $SrFeO_2F$ using a standard top-contact gating architecture. The results for $SrFeO_{3-\delta}$ are presented in **Figure 1a**. The top-contacted architecture is shown in **Figure 1a** (left), in which an initially brownmillerite $SrFeO_{2.5}$ film on a (001)-oriented $(LaAlO_3)_{0.3}(Sr_2AlTaO_6)_{0.7}$ (LSAT) substrate is affixed to an alumina support plate and Ag electrodes are applied from colloidal paint to the edge of the film as a film "top contact." An ion gel of 1-ethyl-3-methylimidazolium bis(trifluoromethylsulfonyl)imide (EMIM TFSI) in poly(vinylidene fluoride-co-hexafluoropropylene) [P(VDF-HFP)] then bridges the contact/film and gate electrode. As illustrated in **Figure 1a** (left), applying a negative gate bias (V_g) is found to drive oxygen into the film, partially oxidizing to perovskite $SrFeO_{3-\delta}$. Supporting this, the voltage dependence for fixed 1 h gating times is shown *via* specular X-ray diffraction (XRD) and optical absorption spectra measured from ellipsometry (**Figure 1a** center and right, respectively). There is little evidence of oxidation until the applied bias exceeds -2 V in magnitude. At -3 V and -4 V gate biases, however, there is a clear shift and broadening of the XRD film peak, from the as-grown pseudocubic (002) $SrFeO_{2.5}$ peak at ~45.1 degrees (*c*-axis lattice parameter = 4.01 Å) toward higher angle, corresponding to a lattice contraction indicative of $SrFeO_{3-\delta}$ oxidation. Corroborating this behavior in the absorption spectra is the development of a low-energy absorption feature at ~1.5 eV, which has been attributed to a mid-bandgap hole-doped state in $SrFeO_{3-\delta}$[51], as well as an evident red-shift in the spectral weight of absorptive intensity as previously reported *via* thermal treatment[41]. To quantify the oxidation, the XRD pattern obtained from -3 V gating was modeled as a bilayer of perovskite $SrFeO_{3-\delta}$ overlaying brownmillerite $SrFeO_{2.5}$. The simulation and resultant bilayer structure are shown in **Figure 1b**, in which the gating resulted in the top 20 unit cells (~8 nm) of the film being oxidized, with an obtained *c*-axis parameter of 3.88 Å on this LSAT substrate. Based on this lattice parameter and optical absorption characteristics, we estimate the oxygen deficiency in this phase to be $\delta \approx 0.14$; see Supplemental Note 1 and **Figure S1** in the supplemental information for more details on this estimate. Attempts to then reduce such films at positive bias were unsuccessful, an issue that will be resolved later in this paper. However, annealing in air at 200 °C did indeed thermally reduce the films to recover the original brownmillerite structure (**Figure S2**), without evidence of degradation, a previously reported concern with ionic gating of perovskites[21,52].

In stark contrast, attempts to oxidize $SrFeO_2F$ films at these voltages with the same device architecture (**Figure 1c, left**) revealed $SrFeO_2F$ to be remarkably robust to

electrochemical oxidation, as evidenced by no significant change to the film structure from XRD (**Figure 1c, center**) or optical properties (**Figure 1c, right**). We show below that this finding extends to electrochemical reduction also, *i.e.*, $SrFeO_2F$ films are essentially inert with respect to ion-gel-gating-induced electrochemistry. We are not aware of any previous work on electrolytic gating of perovskite oxyfluorides, and we can thus only hypothesize as to why $SrFeO_2F$ is largely unchanged under ion gel gating while $SrFeO_{3-\delta}$ is readily electrochemically modified. The propensity for Fe-based perovskites to take on a nominally 3+ oxidation state provides one thermodynamic argument for the stability of $SrFeO_2F$. However, recent analysis of ionic gating has generated strong evidence that it is the anion *diffusivities*, not the anion vacancy formation energies, that dictate whether an oxide exhibits strong electrochemical response to electrolytic gating[53]. While clearly the diffusivity of O^{2-} and F^- anions within $SrFeO_{3-\delta}$ are appreciable as both redox and fluoridation reactions can be carried out topochemically at low temperatures, we hypothesize that the ionic diffusion rate must decrease dramatically once $SrFeO_{2.5}$ is transformed to $SrFeO_2F$. We hypothesize that the removal of significant concentrations of anion vacancies and the formation of strong Fe-F bonds likely play key roles in this apparently decreased diffusivity, and the resultant lack of electrochemical response to ionic gating. This highlights the need for future studies comparing the electrolyte gate responses of oxyfluorides at different O:F ratios, anion vacancy concentrations, and cationic compositions.

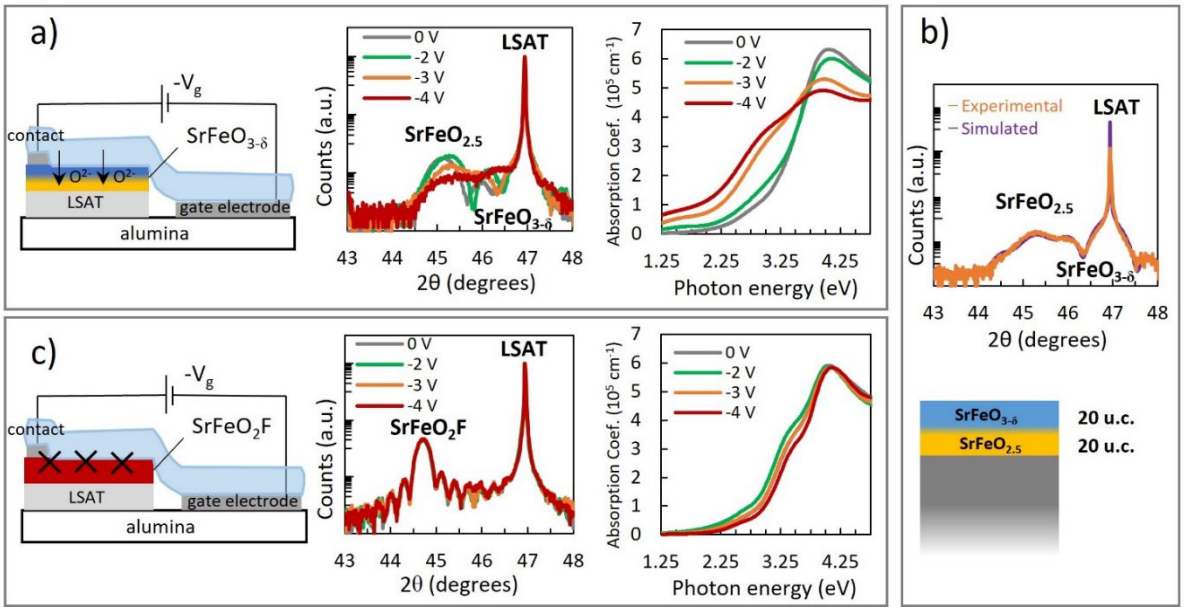

Figure 1. a) Ion gel gating of $SrFeO_{3-\delta}$. A schematic (left) of the top-contact architecture where the ion gel (light blue) bridges the side gate electrode, the oxide film, and the top contact. Specular XRD patterns (center) of films gated at increasingly negative biases for 1 h. Corresponding optical absorption spectra (right). b) Specular XRD pattern and simulated fit for an $SrFeO_{3-\delta}$ film oxidized under -3 V gate bias (for 1 h). The sample structure obtained from the simulation is pictured below: a stack of 20 unit cells of partially oxidized $SrFeO_{3-\delta}$ atop 20 unit cells of $SrFeO_{2.5}$. c) The same information as in (a), but instead with an $SrFeO_2F$ film (red).

To use the above to demonstrate modulation of lateral metal-insulator patterns, we next patterned $SrFeO_{2.5}/SrFeO_2F$ structures using a process similar to that which we previously reported[49], with more details given in the *Materials and Methods* section. In short, a patterned Cr hard-mask was deposited on a $SrFeO_{2.5}$ film, after which the film was subjected to fluoridation topochemistry, and then the mask was subsequently etched to obtain a $SrFeO_{2.5}/SrFeO_2F$ 100-μm-striped pattern. These films were then gated using the same top-contact architecture illustrated in **Figure 1**. The results of gating these films with negative bias (oxidation) for 1 h are illustrated in **Figure 2a**, whereby increasingly negative gate bias more completely oxidizes the oxide regions, while the oxyfluoride regions remain unaffected. This was corroborated by XRD experiments in which the oxyfluoride peak remained unshifted and unaffected, while the oxide film peak displayed oxidative lattice contraction (**Figure S3**). Photographic images of patterned and gated films are shown in **Figure 2b**, in which increasingly negative bias is seen to clearly develop metallic (visibly darkened) oxidized $SrFeO_{3-\delta}$ stripes, while the oxyfluoride regions remain transparent and insulating.

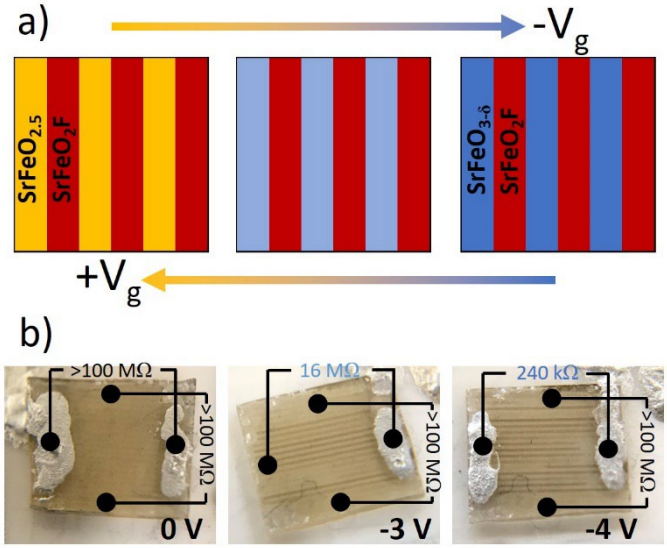

Figure 2. a) Schematic of strategy for voltage-control of laterally patterned heteroanionic materials using ion gel gating, in which oxide ($SrFeO_{3-\delta}$) regions are oxidized by negative bias (moving to the right) and reduced by positive bias (moving to the left), while oxyfluoride ($SrFeO_2F$) regions remain unaffected. b) Images and annotated directional resistance values for heterostructures gated using a top-contact geometry at 0 V (ungated), -3 V, and -4 V for 1 h.

In this geometry, anisotropic electronic transport was then established by two-point probe measurements parallel to the patterned oxide stripes, and perpendicular across the oxide/oxyfluoride stripes, with the results annotated in **Figure 2b**. In all cases, the resistance measured perpendicular to the stripe pattern was >100 MΩ and could not be measured in our setup. Without biasing ("0 V"), the resistance parallel to the stripes also read >100 MΩ, as expected given that both $SrFeO_2F$ and $SrFeO_{2.5}$ are insulators. In contrast, -3 V gate bias yielded a parallel resistance of 16 MΩ and -4 V gating yielded parallel resistance of 240 kΩ, resulting in resistance anisotropy of at least three orders of magnitude (although the true anisotropy is likely greater due to the lead resistance in the two-point measurement) and demonstrating voltage tunability of anisotropic in-plane electronic transport.

As illustrated in **Figure 2a**, positive gate bias would be expected to induce reduction of the oxide to recover the brownmillerite phase of $SrFeO_{2.5}$, but this was not found, even at +3 V. However, under an optical microscope, it was evident that the oxide regions within a few 100 μm of the top contact did reduce upon positive gating, as shown in **Figure S4**. While positive-bias-induced reductive gating has been reported using a top contact geometry in cobaltites, manganites, and nickelates, $SrFeO_{2.5}$ is orders of magnitude more resistive than the oxygen-deficient phases of those materials, such as brownmillerite $SrCoO_{2.5}$. Therefore, the lateral bias dissipation from the contact electrode occurs within drastically shorter distances in the presently

studied samples. The only report of a top-contact-gated ferrite that we are aware of in fact used an only 200-µm-wide channel[34].

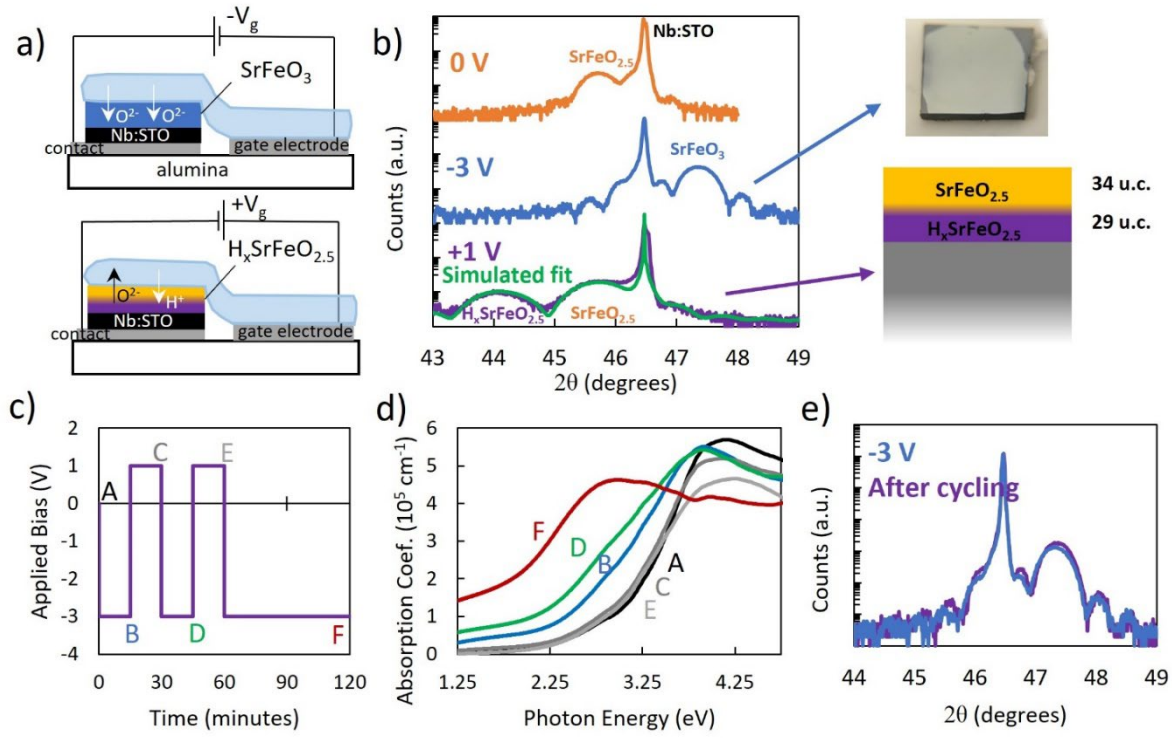

Figure 3. a) Gating schematics of bottom-contacted films showing oxidation with negative bias (top) and reduction with positive bias (bottom). b) Specular XRD patterns from the pristine $SrFeO_{2.5}$ film on Nb:STO substrate (orange), the film after -3 V ion gel gating for 1 h (blue) with an associated image, and the film after +1 V ion gel gating for 1 h (purple) with simulated diffraction data (purple) indicating the film bilayer structure of 34 unit cells of $SrFeO_{2.5}$ atop 29 unit cells of what we assign as $H_xSrFeO_{2.5}$. c) A schematic of the applied bias for the cycling experiment. d) Optical absorption spectra of the film at each indicated stage in the cycling experiment, labeled A-F in (c) and (d). e) Specular XRD pattern of a reference film gated at -3 V for 1 h (blue) and of the cycled film at point F, after the final oxidation (purple).

To facilitate a more uniform electric field distribution at the interface between the ionic gel and the oxide film, we turned to the conductive substrate niobium-doped $SrTiO_3$ (Nb:STO) for use in a bottom-contact architecture. This bottom-contact gating architecture is illustrated in **Figure 3a**. In this geometry, we begin with monolithic $SrFeO_{2.5}$ films grown on conductive (001)-oriented Nb:STO substrates that are affixed to the alumina support plate with silver paint, which serves as a contact electrode. The bias is thus applied from the substrate-film interface, evenly across the film, instead of at the film surface edge. This results in two advantages *versus* top-contact gating: it enables more complete oxidation of $SrFeO_{2.5}$ films at negative gate bias (**Figure 3a, top**) as the field gradient penetrates the entire depth of the film, and it enables reduction at positive bias (**Figure 3a, bottom**) as the field dissipation due to $SrFeO_{2.5}$ resistive screening is limited to the nm-scale thickness of the film. To our knowledge, bottom-contact

gating of $SrFeO_{3-\delta}$ films has been reported only once before, using the conductive buffer layer $(La,Sr)MnO_3$ on a $SrTiO_3$ substrate; the authors reported virtually complete and reversible oxidation and reduction between perovskite $SrFeO_3$ and brownmillerite $SrFeO_{2.5}$[33]. **Figure 3b** shows the XRD patterns from ungated $SrFeO_{2.5}$ (top), after -3 V gating for 1 h (middle), and after +1 V gating for 1 h (bottom). The *c*-axis parameter of the film after -3 V gating is 3.82 Å, which corresponds to fully oxidized $SrFeO_3$ on $SrTiO_3$[54]. While the substrate is black and it is therefore difficult to view a color change in the film, there is also a visible increase in the film reflectance with this oxidation, as seen in the image in **Figure 3b** of the oxidized film, wherein the top right and left corners were not in contact with the ion gel during gating and therefore remain brownmillerite $SrFeO_{2.5}$ and less reflective. In addition, positive-bias gating completely reduces the film in this architecture (**Figure 3b**), even at the rather low voltage of +1 V. The result is in fact *two* film peaks, one corresponding to $SrFeO_{2.5}$ (*c*-axis lattice parameter = 3.96 Å), and the other corresponding to a heavily expanded lattice parameter (*c*-axis lattice parameter = 4.11 Å). We attribute this latter phase to hydrogenated $H_xSrFeO_{2.5}$, which has been reported once in ionically-gated strontium ferrite[4] as well as in several studies involving the analogous $H_xSrCoO_{2.5}$ system[12–14]. While we do not quantify the hydrogen content, *x*, in these films, previous studies with cobaltite films reported an approximate 4.2% *c*-axis lattice parameter expansion on $SrTiO_3$ substrates upon incorporation of one equivalent of hydrogen, as measured by time-of-flight secondary ion mass spectrometry[13,55], in excellent agreement with the lattice expansion we observe in these films (3.8%). Future studies could investigate the quantitative hydrogenation of ferrite films by this method. As indicated in **Figure 3b**, XRD simulation reveals the resulting film structure to consist of a bilayer of 34 unit cells of $SrFeO_{2.5}$ atop 29 unit cells of $H_xSrFeO_{2.5}$. This bilayer structure can be explained by the high mobility of protons through the brownmillerite lattice, meaning that the limiting kinetic step is proton injection from the ion gel into the oxide film, followed by fast diffusion, leading to the buried hydrogenated layer geometry. This deduction of a hydrogenated phase near the substrate interface is supported by depth-dependent XPS measurements (**Figure S5**), which show a slight shift to lower binding energy in the Fe 2*p* spectrum, indicating reduction from Fe^{3+} in $SrFeO_{2.5}$ toward Fe^{2+} in $H_xSrFeO_{2.5}$. Interestingly, XPS also shows the evolution of an Fe^0 signal concomitant with the $H_xSrFeO_{2.5}$ phase, though this remains unexplained.

The mechanism of proton injection in top-contact gating *versus* bottom-contact gating has also been well-described for cobaltite films[13]. In short, in the top-contact architecture, protons are generated from the ionization of water present in the electrolyte (a process that also generates the reservoir of oxygen needed for reoxidation at negative gate voltages) and then

accumulate at the film surface, where the bias is being applied, with relatively little electrostatic driving force for injection into the depth of the film. Alternatively, bottom-contact gating drives protons through the depth of the film to accumulate at the film-substrate interface and therefore convert the oxide phase to the hydrogenated phase. This understanding is especially important as surface degradation of perovskites in contact with ion liquids/gels has been reported previously[21,52], and may be exacerbated by proton accumulation due to acid-base reactivity of perovskite oxides. In particular, $SrFeO_{3-\delta}$ is highly sensitive to strongly acidic environments, which plays a vital role in the design of lithographic processing. Namely, the metal hard mask of choice (here, Cr) is strongly influenced by the need for a chemical etchant that does not contain strong acids. As an example, we use Cr etchant 1020AC which is comprised of an oxidant and acetic acid, whereas Cr etchant 1020, which instead uses nitric acid, fully decomposes the $SrFeO_{3-\delta}$ film. Additionally, reductive gating at +2 V and greater resulted in decomposition of the $SrFeO_{3-\delta}$ film, which we speculate may be due to proton accumulation and acid-catalyzed breakdown.

Having established that bottom-contact gating enables full oxidation and reduction of $SrFeO_{3-\delta}$ films at moderate voltages (-3 V and +1 V, respectively), we next tested the reversibility of the gating under voltage cycling, as shown in **Figure 3c**. Points A-F indicated in this figure correspond to the ungated $SrFeO_{2.5}$ film, and films after 15 min of gating at -3 V and +1 V in succession for two cycles, followed by a final oxidative gating for 1 h. The film progression was monitored by absorption spectra measured by ellipsometry, as displayed in **Figure 3d** with the spectra labelled by their corresponding stage in the cycling (A-E). Oxidative gating for 15 min resulted in partial oxidation of the films (B, D), and 15 min reductive gating regained the fully reduced films (C, E). The final hour-long oxidation then resulted in an absorption spectrum corresponding to fully oxidized $SrFeO_3$, corroborated by XRD (**Figure 3e,** "after cycling"). Furthermore, the XRD pattern of the cycled film is compared to a non-cycled oxidized film in **Figure 3e**, showing that there is negligible degradation of the film, which would manifest as film peak broadening, etc.

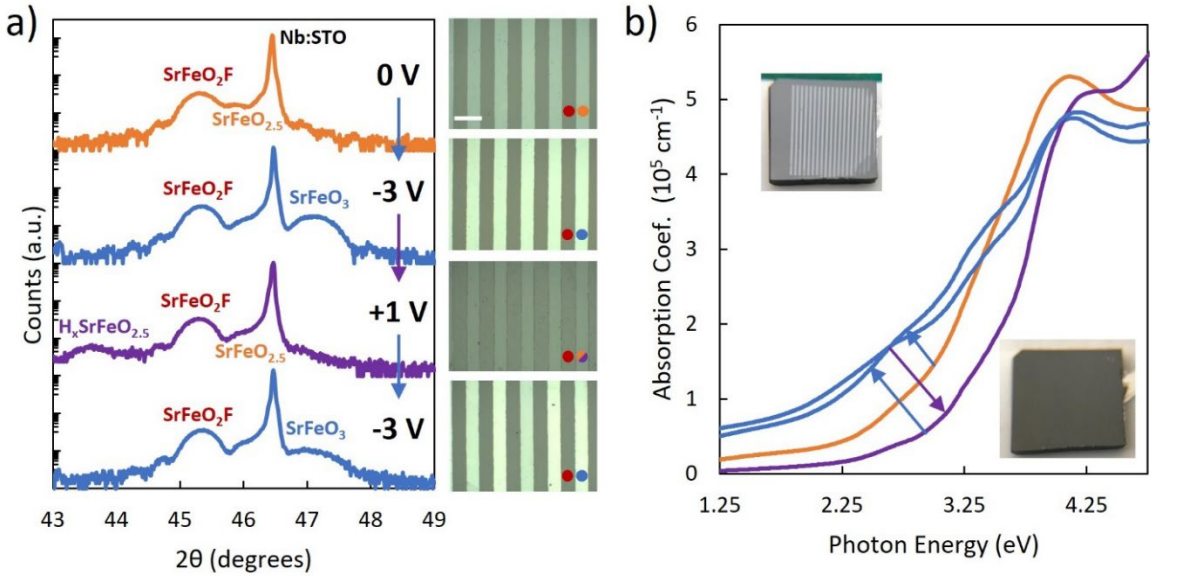

Figure 4. a) Specular XRD patterns of a cycled ion-gel-gated $SrFeO_2F/SrFeO_{3-\delta}$ heterostructure of patterned 100 μm stripes. From top to bottom: the as-patterned $SrFeO_2F/SrFeO_{2.5}$ film (orange), the $SrFeO_2F/SrFeO_3$ film after -3V gating for 30 min (blue), the $SrFeO_2F/H_xSrFeO_{2.5}$ film after +1V gating for 30min (purple), and the $SrFeO_2F/SrFeO_3$ film after -3V gating for 30 min (blue). To the right of the XRD data are optical microscope images of the corresponding lateral heterostructures; the scale bar in the first image is 200 μm. Regions are denoted by the color-coded markings: red for $SrFeO_2F$, orange for $SrFeO_{2.5}$, blue for $SrFeO_3$, and orange/purple for $H_xSrFeO_{2.5}$. b) Optical absorption data (color-coded) measured at each stage of the process described above. Inset: photographs of the $SrFeO_2F/SrFeO_3$ heterostructure (top-left) and $SrFeO_2F/H_xSrFeO_{2.5}$ (bottom-right).

We also tested the reversibility of ion gel gating of $SrFeO_2F/SrFeO_{3-\delta}$ lateral heterostructures in the bottom-contact geometry. **Figure 4a** displays the specular XRD data and corresponding optical microscope images of laterally-patterned samples in the following states (from top to bottom): ungated, oxidatively gated, reductively gated, and oxidatively re-gated films, at -3 V and +1 V for oxidation and reduction, respectively. Throughout this cycling, the $SrFeO_2F$ film peak remains unchanged (*c*-axis lattice parameter = 3.99 Å), while the $SrFeO_{3-\delta}$ peak shifts between that of $SrFeO_3$ and $SrFeO_{2.5}/H_xSrFeO_{2.5}$. Due to the reflective nature of metallic $SrFeO_3$, oxidized $SrFeO_3$ appears brighter in the optical microscope images, while insulating reduced $H_xSrFeO_{2.5}$ and $SrFeO_2F$ appear darker. We note that the initial ungated heterostructure here has slightly oxidized $SrFeO_{3-\delta}$ regions likely due to the oxidative Cr etching solution used in the patterning process. We also note that there is a slight broadening of the $SrFeO_3$ peak in the final XRD pattern; we speculate that this is due to too long a duration (30 min) of the reductive gating step for reasons discussed earlier, *i.e.,* that excessive proton accumulation from positive gating can acid-catalyze the degradation of perovskite oxides, while shorter gating times (as in **Figure 3**) resulted in no noticeable degradation. Resulting optical

properties of these lateral heterostructures are shown in **Figure 4b**. The absorption spectra show the initial shift toward low-energy absorption due to oxidation, and the top left inset image shows the reflectivity of $SrFeO_3$ stripes in the oxidized film. Cycling to positive bias and subsequent reduction of the oxide stripes shows recovery of the fully insulating film in the absorption spectrum as well as the visible erasure of the metal-insulator pattern (see the image in the bottom right inset).

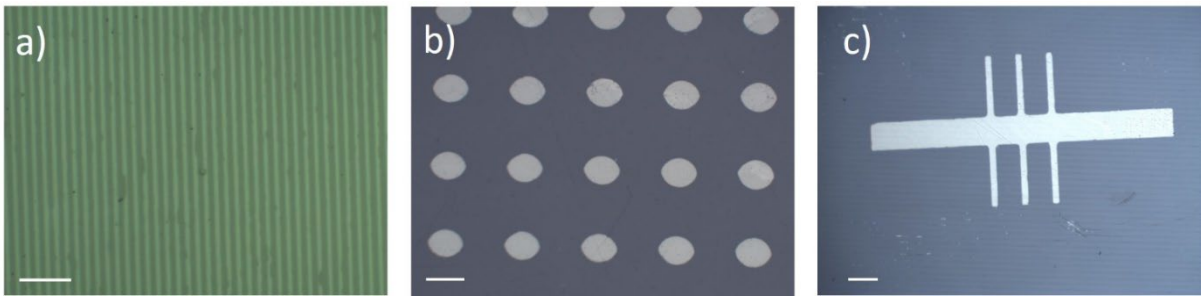

Figure 5. a) Optical microscope image of a 2 μm striped heterostructure of $SrFeO_3/SrFeO_2F$. Scale bar = 20 μm. b) Optical microscope image of columnar structured $SrFeO_3$ within a $SrFeO_2F$ matrix. Scale bar = 100 μm. c) Optical microscope image of a patterned Hall bar of $SrFeO_3$ in a $SrFeO_2F$ matrix. Scale bar = 100 μm. Brighter regions correspond to $SrFeO_3$ and darker regions correspond to $SrFeO_2F$.

While demonstrated here for a single pattern-type (stripes) and materials family (ferrites), this work holds implications for electric-field control over a variety of structures and functions. The lateral patterning used here is based on photolithographically-defined regions that are topochemically converted to oxyfluorides. Therefore, the structures are not limited to stripes but can instead take on much more complex or arbitrary shapes, as might be required for optical, magnetic media, or metamaterial-based devices. For instance, we have patterned $SrFeO_2F/SrFeO_{2.5}$ samples into 2 μm lateral heterostructures, isolated columns of $SrFeO_3$ within a $SrFeO_2F$ matrix, and defined $SrFeO_3$ Hall bar geometries amidst $SrFeO_2F$ (**Figure 5**). We show in this work that this approach enables voltage-tunable in-plane electronic anisotropy by altering the oxygen content within the $ABO_{3-\delta}$ stripes running parallel to the conduction direction. While not demonstrated here, we hypothesize that the spatial selectivity of *ionic* conductivity (as in the case of oxygen herein or other cationic-diffusive oxides such as VO_2[56], WO_3[57,58], perovskite nickelates[36], and perovskite ruthenates[59,60]), as well as *thermal* conductivity[61,62], could be similarly controlled by gate-induced electrochemical transformations. This would enable reversible and dynamic control of charge or heat flow for Mottronic[63,64] and thermal devices[65], respectively.

In future studies, we anticipate that this approach can be expanded to other material systems amenable to fluoridation, such as cobaltites[66,67], manganites[68–70], chromites[71],

nickelates[72], and ruthenates[73]. While F is particularly useful for topochemical modification of the nature used here, it is also possible that other halides, pnictides, and chalcogenides could be used in a similar manner. Additionally, while a conductive, opaque substrate was used in this study to enable complete and homogeneous conversion between conductive and insulating phases of strontium ferrite, we recognize that some applications may necessitate optical transparency of the substrate or electrical isolation of the film. For these purposes, future studies could employ a transparent, non-conductive substrate and attain electrochemical conversion using elevated temperature[74], a transparent conductive buffer layer[75], or simply an insulating and electrochemically-inert buffer layer (*e.g.* $LaFeO_3$) between a conductive substrate and the active film for devices where only electrical isolation from the substrate is required. Finally, we note that while the side-gating architecture used in this study lends itself to rapid exploratory work, the resulting mm-scale distance between the gate electrode and channel results in long gating times. Alternatively, it has been shown that the electric double layer can be modulated in the kHz to MHz frequency regime in devices with a superstrate gate electrode[76], which warrants future studies on the switching speeds afforded by top-gated geometries.

3. Conclusion

We have shown that ion gel gating of lateral oxide/oxyfluoride heterostructures enables spatially-selective voltage-based control of metal/insulator properties in perovskite thin films. In these structures, $SrFeO_2F$ layers do not exhibit any measurable oxidation or reduction upon biasing. In contrast, bottom-contact gating enables full oxidation of the $SrFeO_{3-\delta}$ regions to metallic $SrFeO_3$, and reduction to insulating $H_xSrFeO_{2.5}$. This enables new design strategies for optoelectronic and magnetic oxide-based devices in which lateral optical contrast or in-plane anisotropy of functional properties can be tuned at room temperature, and with modest applied voltages, with little power dissipation.

4. Materials and Methods

Thin Film Growth. 5 x 5 mm^2 $SrFeO_{2.5}$ epitaxial thin films were grown by oxygen-assisted molecular beam epitaxy (MBE). (001)-oriented single-crystal substrates of $(LaAlO_3)_{0.3}(Sr_2TaAlO_6)_{0.7}$ (LSAT) or Nb:$SrTiO_3$ (Nb:STO) (MTI Corporation) were heated in vacuum to ~600 °C for deposition. Knudsen cells containing Sr (99.95%, Alfa Aesar) and Fe (99.95%, Alfa Aesar) were heated to ~450 °C and ~1200 °C, respectively. Material effusion rates were calibrated using a quartz crystal microbalance. The chamber pressure was maintained

at ~5 x 10^{-6} Torr of O_2 and films were deposited by co-deposition from the above sources for ~30 s per monolayer with a 10 s anneal in between layers. Films were grown to between 40 and 80 unit cells thick (~16-32 nm).

Fluoridation Topochemistry. Fluoridation reactions were performed in a quartz tube furnace as reported previously[49,77]. Films were placed in an Al boat, downstream of poly(vinylidene fluoride) (PVDF) pellets. The boat was wrapped in foil and ingress and egress holes were punctured in the foil to allow for gas exchange. The boat was placed in the tube furnace and inert carrier gas (Ar) purged the setup for 5 min at 1 liter per min flow rate. The flow rate was then decreased and the temperature of the furnace was raised to 230 °C at a rate of 12 °C/min, and allowed to remain at temperature for 1 h. The furnace was then cooled to room temperature at 30 °C/min under Ar flow. X-ray diffraction and optical characterization corroborated the anion stoichiometry of the resultant phase to be approximately $SrFeO_2F$[49,77].

Sample Patterning. Samples were patterned using photolithography in a process adapted from our previous work[49]. KL 5315 (KemLab) photoresist was first spun onto samples at 4,000 RPM for 30 s, then soft-baked at 100 °C for 1 min. Exposure was performed through a shadow mask using an MJB3 Mask Aligner (Karl Suss), with a dose of 25 mW/cm^2 of 405 nm light for a duration of 3.2 s. Development was performed by submerging the sample in 2.38% w/w aqueous tetramethylammonium hydroxide (Alfa Aesar) for 30 s, followed by 30 s of gentle agitation, and finally drying under a N_2 stream. A hard mask of Cr was then deposited by DC sputtering at a pressure of 3 mTorr of Ar at 100 W for 5-10 min. Liftoff of the remaining photoresist was achieved by sonication in acetone. The resultant Cr-hard-masked films were then subjected to fluoridation as described above. Finally, the Cr mask was etched with Cr Etchant 1020AC (Transene).

Ion Gel Gating. Films were electrochemically gated in both top- and bottom-contacted geometries, as outlined in the main section of this paper. For the top-contact geometry, $SrFeO_{3-\delta}$ on (insulating) LSAT substrates were affixed to alumina plates, and Ag electrodes were applied to the edge of the films and on the alumina plates with colloidal silver paint (Ted Pella). For the bottom-contact geometry, $SrFeO_{3-\delta}$ on (conductive) Nb:STO substrates were affixed to alumina plates using colloidal silver paint – this paint also served as the back contact – and a separate electrode of Ag was also applied to the plate. Ion gels composed of 1-ethyl-3-methylimidazolium bis(trifluoromethylsulfonyl)imide (EMIM TFSI) in a P(VDF-HFP) matrix were used as the electrolyte. Gels were placed to cover the films as well as the gate electrode

on the alumina plate, and a DC voltage was applied between the electrodes to perform ion gel gating at room temperature in ambient atmosphere.

Materials Characterization. Specular X-ray diffraction (XRD) measurements were performed on a Rigaku SmartLab diffractometer in high-resolution mode with a Ge double-bounce monochromator. Resistance measurements were carried out by two-point probe means, using a Hewlett Packard 34401A multimeter. Optical absorption was measured by variable angle spectroscopic ellipsometry (J. A. Woollam M2000-U) in the angular range from 65° to 75°. X-ray photoelectron spectroscopy (XPS) was performed with a PHI VersaProbe 5000, using Ar^+ and e^- flood guns for charge neutralization, as well as Ar^+ sputtering for depth profiling. All characterization was carried out after removal of the ion gel from the sample surface and swabbing of the film with acetone and isopropanol to remove any residue from the gel.

Statistical Analysis. X-ray diffraction data were modeled and fit using using GenX[78]. Variable angle spectroscopic ellipsometry data were modeled and fit using CompleteEase software (J. A. Woollam) according to the following procedure. Bare LSAT and Nb:STO substrates were measured and modeled with a Cauchy and general oscillator dispersion models, respectively. Thin-film samples were modeled, and n and k extracted, using B-spline fits in accordance with the Kramers-Kronig relationship of real and imaginary parts of the refractive index. The optical absorption coefficient was calculated as $\alpha = 4\pi k\lambda^{-1}$, where λ is the photon wavelength.

Supporting Information

Supporting Information is available from the Wiley Online Library or from the author.

Acknowledgments

B.M.L. and S.J.M. were supported by the National Science Foundation, under grant number CMMI-2001888. W.M.P. and C.L. were supported by the National Science Foundation through the University of Minnesota MRSEC under award number DMR-2011401. XRD and XPS analyses were performed using instruments in the Materials Characterization Core at Drexel University.

Conflict of Interest

The authors declare no conflict of interest.

Data Availability Statement

The data that support the findings of this study are available from the corresponding author upon reasonable request.

Received: ((will be filled in by the editorial staff))
Revised: ((will be filled in by the editorial staff))
Published online: ((will be filled in by the editorial staff))

References

[1] C. Leighton, *Nat. Mater.* **2019**, *18*, 13.

[2] S. Z. Bisri, S. Shimizu, M. Nakano, Y. Iwasa, *Adv. Mater.* **2017**, *29*, 1607054.

[3] J. H. Cho, J. Lee, Y. Xia, B. Kim, Y. He, M. J. Renn, T. P. Lodge, C. Daniel Frisbie, *Nat. Mater.* **2008**, *7*, 900.

[4] Y. Isoda, D. Kan, Y. Ogura, T. Majima, T. Tsuchiya, Y. Shimakawa, *Appl. Phys. Lett.* **2022**, *120*, 091601.

[5] H. Ohta, Y. Sato, T. Kato, S. Kim, K. Nomura, Y. Ikuhara, H. Hosono, *Nat. Commun.* **2010**, *1*, 118.

[6] T. Katase, Y. Suzuki, H. Ohta, *J. Appl. Phys.* **2017**, *122*, 135303.

[7] D. Wang, L. Meng, L. Wei, P. Shi, Y. Chen, S. Yan, Y. Tian, G. Liu, L. Mei, *J. Magn. Magn. Mater.* **2020**, *496*, 165926.

[8] P. Shi, D. Wang, T. Yu, R. Xing, Z. Wu, S. Yan, L. Wei, Y. Chen, H. Ren, C. Yu, F. Li, *Mater. Des.* **2021**, *210*, 110022.

[9] D. Wang, S. Zhao, R. Yin, L. Li, Z. Lou, G. Shen, *npj Flex. Electron.* **2021**, *5*, 13.

[10] J. Jeong, N. Aetukuri, T. Graf, T. D. Schladt, M. G. Samant, S. S. P. Parkin, *Science* **2013**, *339*, 1402.

[11] T. D. Schladt, T. Graf, N. B. Aetukuri, M. Li, A. Fantini, X. Jiang, M. G. Samant, S. S. P. Parkin, *ACS Nano* **2013**, *7*, 8074.

[12] N. Lu, P. Zhang, Q. Zhang, R. Qiao, Q. He, H.-B. Li, Y. Wang, J. Guo, D. Zhang, Z. Duan, Z. Li, M. Wang, S. Yang, M. Yan, E. Arenholz, S. Zhou, W. Yang, L. Gu, C. Nan, J. Wu, Y. Tokura, P. Yu, *Nature* **2017**, *546*, 124.

[13] H. Li, F. Lou, Y. Wang, Y. Zhang, Q. Zhang, D. Wu, Z. Li, M. Wang, T. Huang, Y. Lyu, J. Guo, T. Chen, Y. Wu, E. Arenholz, N. Lu, N. Wang, Q. He, L. Gu, J. Zhu, C. Nan, X. Zhong, H. Xiang, P. Yu, *Adv. Sci.* **2019**, *6*, 1901432.

[14] Q. Yang, J. Lee, H. Jeen, H. J. Cho, H. Ohta, *ACS Appl. Electron. Mater.* **2021**, *3*, 3296.

[15] Y. He, S. Jiang, C. Chen, C. Wan, Y. Shi, Q. Wan, *J. Appl. Phys.* **2021**, *130*, 190904.

[16] H. Huang, C. Ge, Z. Liu, H. Zhong, E. Guo, M. He, C. Wang, G. Yang, K. Jin, *J. Semicond.* **2021**, *42*, 013103.

[17] M. Nichterwitz, S. Honnali, M. Kutuzau, S. Guo, J. Zehner, K. Nielsch, K. Leistner, *APL Mater.* **2021**, *9*, 030903.

[18] U. Bauer, L. Yao, A. J. Tan, P. Agrawal, S. Emori, H. L. Tuller, S. van Dijken, G. S. D. Beach, *Nat. Mater.* **2015**, *14*, 174.

[19] C. Bi, Y. Liu, T. Newhouse-Illige, M. Xu, M. Rosales, J. W. Freeland, O. Mryasov, S. Zhang, S. G. E. te Velthuis, W. G. Wang, *Phys. Rev. Lett.* **2014**, *113*, 267202.

[20] J. S. Lim, J. Lee, B. J. Lee, Y.-J. Kim, H.-S. Park, J. Suh, H.-H. Nahm, S.-W. Kim, B.-G. Cho, T. Y. Koo, E. Choi, Y.-H. Kim, C.-H. Yang, *Sci. Adv.* **2020**, *6*, 1.

[21] J. Walter, H. Wang, B. Luo, C. D. Frisbie, C. Leighton, *ACS Nano* **2016**, *10*, 7799.

[22] J. Walter, G. Yu, B. Yu, A. Grutter, B. Kirby, J. Borchers, Z. Zhang, H. Zhou, T. Birol, M. Greven, C. Leighton, *Phys. Rev. Mater.* **2017**, *1*, 071403.

[23] B. Cui, P. Werner, T. Ma, X. Zhong, Z. Wang, J. M. Taylor, Y. Zhuang, S. S. P. Parkin, *Nat. Commun.* **2018**, *9*, 3055.

[24] S. Ning, Q. Zhang, C. Occhialini, R. Comin, X. Zhong, C. A. Ross, *ACS Nano* **2020**, *14*, 8949.

[25] V. Chaturvedi, W. M. Postiglione, R. D. Chakraborty, B. Yu, W. Tabiś, S. Hameed, N. Biniskos, A. Jacobson, Z. Zhang, H. Zhou, M. Greven, V. E. Ferry, C. Leighton, *ACS Appl. Mater. Interfaces* **2021**, *13*, 51205.

[26] Q. Lu, B. Yildiz, *Nano Lett.* **2016**, *16*, 1186.

[27] W. S. Choi, H. Jeen, J. H. Lee, S. S. A. Seo, V. R. Cooper, K. M. Rabe, H. N. Lee, *Phys. Rev. Lett.* **2013**, *111*, 097401.

[28] A. S. Dhoot, C. Israel, X. Moya, N. D. Mathur, R. H. Friend, *Phys. Rev. Lett.* **2009**, *102*, 136402.

[29] B. Cui, C. Song, G. Wang, Y. Yan, J. Peng, J. Miao, H. Mao, F. Li, C. Chen, F. Zeng, F. Pan, *Adv. Funct. Mater.* **2014**, *24*, 7233.

[30] J. Shi, S. D. Ha, Y. Zhou, F. Schoofs, S. Ramanathan, *Nat. Commun.* **2013**, *4*, 2676.

[31] Y. Dong, H. Xu, Z. Luo, H. Zhou, D. D. Fong, W. Wu, C. Gao, *APL Mater.* **2017**, *5*, 051101.

[32] A. L. Krick, S. J. May, *APL Mater.* **2017**, *5*, 042504.

[33] M. S. Saleem, B. Cui, C. Song, Y. Sun, Y. Gu, R. Zhang, M. U. Fayaz, X. Zhou, P. Werner, S. S. P. Parkin, F. Pan, *ACS Appl. Mater. Interfaces* **2019**, *11*, 6581.

[34] C. Ge, C. Liu, Q. Zhou, Q. Zhang, J. Du, J. Li, C. Wang, L. Gu, G. Yang, K. Jin, *Adv. Mater.* **2019**, *31*, 1900379.

[35] J. Song, Y. Chen, X. Chen, H. Wang, T. Khan, F. Han, J. Zhang, H. Huang, J. Zhang, H. Zhang, H. Zhang, X. Yan, S. Qi, F. Hu, B. Shen, R. Yu, J. Sun, *Phys. Rev. Appl.* **2019**, *12*, 054016.

[36] J. Shi, Y. Zhou, S. Ramanathan, *Nat. Commun.* **2014**, *5*, 4860.

[37] A. J. Tan, M. Huang, C. O. Avci, F. Büttner, M. Mann, W. Hu, C. Mazzoli, S. Wilkins, H. L. Tuller, G. S. D. Beach, *Nat. Mater.* **2019**, *18*, 35.

[38] M. Huang, A. Jun Tan, F. Büttner, H. Liu, Q. Ruan, W. Hu, C. Mazzoli, S. Wilkins, C. Duan, J. K. W. Yang, G. S. D. Beach, *Nat. Commun.* **2019**, *10*, 5030.

[39] J. de Rojas, A. Quintana, A. Lopeandía, J. Salguero, B. Muñiz, F. Ibrahim, M. Chshiev, A. Nicolenco, M. O. Liedke, M. Butterling, A. Wagner, V. Sireus, L. Abad, C. J. Jensen, K. Liu, J. Nogués, J. L. Costa-Krämer, E. Menéndez, J. Sort, *Nat. Commun.* **2020**, *11*, 5871.

[40] T. Maeder, J. . Bednorz, *J. Eur. Ceram. Soc.* **1999**, *19*, 1507.

[41] A. Khare, D. Shin, T. S. Yoo, M. Kim, T. D. Kang, J. Lee, S. Roh, I. Jung, J. Hwang, S. W. Kim, T. W. Noh, H. Ohta, W. S. Choi, *Adv. Mater.* **2017**, *29*, 1606566.

[42] J. P. Hodges, S. Short, J. D. Jorgensen, X. Xiong, B. Dabrowski, S. M. Mini, C. W. Kimball, *J. Solid State Chem.* **2000**, *151*, 190.

[43] H. D'Hondt, A. M. Abakumov, J. Hadermann, A. S. Kalyuzhnaya, M. G. Rozova, E. V Antipov, G. Van Tendeloo, *Chem. Mater.* **2008**, *20*, 7188.

[44] Z. Li, R. Laskowski, T. Iitaka, T. Tohyama, *Phys. Rev. B* **2012**, *85*, 134419.

[45] J. C. Waerenborgh, E. V. Tsipis, J. E. Auckett, C. D. Ling, V. V. Kharton, *J. Solid State Chem.* **2013**, *205*, 5.

[46] P. Adler, A. Lebon, V. Damljanović, C. Ulrich, C. Bernhard, A. V Boris, A. Maljuk, C. T. Lin, B. Keimer, *Phys. Rev. B* **2006**, *73*, 094451.

[47] A. Lebon, P. Adler, C. Bernhard, A. V Boris, A. V Pimenov, A. Maljuk, C. T. Lin, C. Ulrich, B. Keimer, *Phys. Rev. Lett.* **2004**, *92*, 037202.

[48] S. K. Acharya, R. V. Nallagatla, O. Togibasa, B. W. Lee, C. Liu, C. U. Jung, B. H. Park, J. Y. Park, Y. Cho, D. W. Kim, J. Jo, D. H. Kwon, M. Kim, C. S. Hwang, S. C. Chae, *ACS Appl. Mater. Interfaces* **2016**, *8*, 7902.

[49] B. M. Lefler, T. Duchoň, G. Karapetrov, J. Wang, C. M. Schneider, S. J. May, *Phys.*

Rev. Mater. **2019**, *3*, 073802.

[50] T. Katayama, A. Chikamatsu, H. Kamisaka, H. Kumigashira, T. Hasegawa, *Appl. Phys. Express* **2016**, *9*, 025801.

[51] H. Wadati, D. Kobayashi, H. Kumigashira, K. Okazaki, T. Mizokawa, A. Fujimori, K. Horiba, M. Oshima, N. Hamada, M. Lippmaa, M. Kawasaki, H. Koinuma, *Phys. Rev. B* **2005**, *71*, 035108.

[52] A. C. Lang, J. D. Sloppy, H. Ghassemi, R. C. Devlin, R. J. Sichel-Tissot, J.-C. Idrobo, S. J. May, M. L. Taheri, *ACS Appl. Mater. Interfaces* **2014**, *6*, 17018.

[53] C. Leighton, T. Birol, J. Walter, *APL Mater.* **2022**, *10*, 040901.

[54] Y. J. Xie, M. D. Scafetta, E. J. Moon, A. L. Krick, R. J. Sichel-Tissot, S. J. May, *Appl. Phys. Lett.* **2014**, *105*, 062110.

[55] H.-B. Li, S. Kobayashi, C. Zhong, M. Namba, Y. Cao, D. Kato, Y. Kotani, Q. Lin, M. Wu, W.-H. Wang, M. Kobayashi, K. Fujita, C. Tassel, T. Terashima, A. Kuwabara, Y. Kobayashi, H. Takatsu, H. Kageyama, *J. Am. Chem. Soc.* **2021**, *143*, 17517.

[56] H. Yoon, M. Choi, T.-W. Lim, H. Kwon, K. Ihm, J. K. Kim, S.-Y. Choi, J. Son, *Nat. Mater.* **2016**, *15*, 1113.

[57] S. Nishihaya, M. Uchida, Y. Kozuka, Y. Iwasa, M. Kawasaki, S. Nishihaya, M. Uchida, Y. Kozuka, Y. Iwasa, M. Kawasaki, Y. Iwasa, M. Kawasaki, *ACS Appl. Mater. Interfaces* **2016**, *8*, 22330.

[58] X. Leng, J. Pereiro, J. Strle, G. Dubuis, A. T. Bollinger, A. Gozar, J. Wu, N. Litombe, C. Panagopoulos, D. Pavuna, I. Božović, *npj Quantum Mater.* **2017**, *2*, 35.

[59] Z. Li, S. Shen, Z. Tian, K. Hwangbo, M. Wang, Y. Wang, F. M. Bartram, L. He, Y. Lyu, Y. Dong, G. Wan, H. Li, N. Lu, J. Zang, H. Zhou, E. Arenholz, Q. He, L. Yang, W. Luo, P. Yu, *Nat. Commun.* **2020**, *11*, 184.

[60] S. Shen, Z. Li, Z. Tian, W. Luo, S. Okamoto, P. Yu, *Phys. Rev. X* **2021**, *11*, 021018.

[61] Q. Lu, S. Huberman, H. Zhang, Q. Song, J. Wang, G. Vardar, A. Hunt, I. Waluyo, G. Chen, B. Yildiz, *Nat. Mater.* **2020**, *19*, 655.

[62] S. Ning, S. C. Huberman, Z. Ding, H. Nahm, Y. Kim, H. Kim, G. Chen, C. A. Ross, *Adv. Mater.* **2019**, *31*, 1903738.

[63] J. Chen, W. Mao, L. Gao, F. Yan, T. Yajima, N. Chen, Z. Chen, H. Dong, B. Ge, P. Zhang, X. Cao, M. Wilde, Y. Jiang, T. Terai, J. Shi, *Adv. Mater.* **2020**, *32*, 1905060.

[64] X. Zhou, H. Li, F. Meng, W. Mao, J. Wang, Y. Jiang, K. Fukutani, M. Wilde, B. Fugetsu, I. Sakata, N. Chen, J. Chen, *J. Phys. Chem. Lett.* **2022**, 8078.

[65] G. Wehmeyer, T. Yabuki, C. Monachon, J. Wu, C. Dames, *Appl. Phys. Rev.* **2017**, *4*,

041304.

[66] T. Katayama, A. Chikamatsu, Y. Hirose, T. Fukumura, T. Hasegawa, *J. Sol-Gel Sci. Technol.* **2015**, *73*, 527.

[67] E. Sullivan, C. Greaves, *Mater. Res. Bull.* **2012**, *47*, 2541.

[68] J. Wang, Y. Shin, E. Arenholz, B. M. Lefler, J. M. Rondinelli, S. J. May, *Phys. Rev. Mater.* **2018**, *2*, 073407.

[69] P. Anitha Sukkurji, A. Molinari, C. Reitz, R. Witte, C. Kübel, V. Chakravadhanula, R. Kruk, O. Clemens, *Materials (Basel).* **2018**, *11*, 1204.

[70] J. Wang, B. M. Lefler, S. J. May, *Inorg. Chem.* **2020**, *59*, 9990.

[71] A. Chikamatsu, T. Maruyama, T. Katayama, Y. Su, Y. Tsujimoto, K. Yamaura, M. Kitamura, K. Horiba, H. Kumigashira, T. Hasegawa, *Phys. Rev. Mater.* **2020**, *4*, 025004.

[72] T. Onozuka, A. Chikamatsu, T. Katayama, Y. Hirose, I. Harayama, D. Sekiba, E. Ikenaga, M. Minohara, H. Kumigashira, T. Hasegawa, *ACS Appl. Mater. Interfaces* **2017**, *9*, 10882.

[73] K. Kawahara, A. Chikamatsu, T. Katayama, T. Onozuka, D. Ogawa, K. Morikawa, E. Ikenaga, Y. Hirose, I. Harayama, D. Sekiba, T. Fukumura, T. Hasegawa, *CrystEngComm* **2017**, *19*, 313.

[74] M. Wang, X. Sui, Y. Wang, Y. Juan, Y. Lyu, H. Peng, T. Huang, S. Shen, C. Guo, J. Zhang, Z. Li, H. Li, N. Lu, A. T. N'Diaye, E. Arenholz, S. Zhou, Q. He, Y. Chu, W. Duan, P. Yu, *Adv. Mater.* **2019**, *31*, 1900458.

[75] H. He, Z. Yang, Y. Xu, A. T. Smith, G. Yang, L. Sun, *Nano Converg.* **2020**, *7*, 32.

[76] F. Zare Bidoky, C. D. Frisbie, *ACS Appl. Mater. Interfaces* **2022**, *14*, 21295.

[77] T. Katayama, A. Chikamatsu, Y. Hirose, R. Takagi, H. Kamisaka, T. Fukumura, T. Hasegawa, *J. Mater. Chem. C* **2014**, *2*, 5350.

[78] M. Björck, G. Andersson, *J. Appl. Crystallogr.* **2007**, *40*, 1174.

Electrolytic gating applied to lateral oxide/oxyfluoride perovskite heterostructures is used to demonstrate dynamic and reversible voltage control over a transition between lithographically defined metal/insulator and insulator/insulator lateral patterns at room temperature. This approach enables electric field modulation of anisotropic electronic transport and optical responses.

B. M. Lefler[1], W. M. Postiglione[2], C. Leighton, S. J. May*

Voltage control of patterned metal/insulator properties in oxide/oxyfluoride lateral perovskite heterostructures *via* ion gel gating